Emergence of active turbulence limits chemotaxis-induced collective condensation of bacteria.

Nir Livne and Ady Vaknin*

The Racah Institute of Physics, The Hebrew University, Jerusalem 91904, Israel

Corresponding author: Ady Vaknin

Email: avaknin@mail.huji.ac.il

Author Contributions: NL and AV designed the experiments; NL performed the experiments and theoretical calculations; NL and AV analyzed the data and wrote the manuscript.

Competing Interest Statement: The authors declare no competing interests.

Classifications:

Biological Sciences

- Biophysics and Computational Biology
- Population Biology
- Microbiology
- Systems Biology

Keywords: Bacterial chemotaxis | Collective condensation | Correlated swimming | Active matter.

Abstract

Collective bacterial condensation arises from positive feedback between the ability of bacteria to generate chemical gradients and their chemotactic ability to track those gradients, resulting in the spontaneous formation of local cell accumulations. Here, by following the bacterial condensation dynamics in uniform acidic environments, we show that condensation is critically constrained by the spontaneous emergence of correlated bacterial swimming. Under the unique conditions prevailing within the condensate—characterized by sharp cell-density gradients and the absence of physical boundaries—correlated bacterial motion leads to vortex-like cell motion with an additional substantial radial component directed down the cell-density gradient. Correlated bacterial motion leads, in turn, to local fluid motion that tends to broaden the condensate and expels non-chemotactic bacteria. However, when cells are embedded in a porous environment, correlated motion is suppressed, allowing spontaneous condensation to proceed further and form exceptionally dense bacterial accumulations. Overall, these findings highlight a previously unrecognized interplay between self-generated bacterial condensation and correlated swimming.

Significance statement

Self-induced condensation and active turbulence are two prominent forms of collective bacterial behaviors. However, their interplay has not been experimentally studied. Here, we show that collective bacterial condensation gives rise to correlated swimming, which in turn fundamentally limits further condensation. Furthermore, we demonstrate that in dilute porous environments—common in natural bacterial habitats—correlated swimming is strongly suppressed, enabling the spontaneous formation of extremely dense cell condensates. These condensates may serve as a basis for the development of more structured bacterial communities.

Introduction

Motile bacteria navigate their environment by tracking chemical gradients toward regions they deem favorable (1-4). This behavior, termed chemotaxis, influences many aspects of bacterial ecology (5, 6) and human health (7-9). Even in spatially uniform environments, bacteria can collectively follow self-generated gradients, allowing them to accelerate their expansion into resource-rich regions (10, 11), or, alternatively, condense into focal points by either secreting beneficial (attractant) effectors (12, 13) or neutralizing harmful (repellent) effectors (14). Notably, in contrast to the inherently dynamic bacterial distributions triggered by external chemoeffector release (15) or in expanding bacterial bands (16), bacterial condensation can lead to sharp but quasi-static bacterial accumulation (14). Condensation relies on positive feedback between self-generated gradients and the chemotactic responses of the bacteria to those gradients (Fig. 1A) that, in principle, can lead to a divergence in the local cell density (17). From studies of low cell-density, transient condensations, it was suggested that a fundamental limit on such cell condensation arises from the fact that chemotaxis itself is a non-local behavior (18). However, the fundamental constraints on stable, high-density bacterial condensations remain unclear. Here, we show that at high cell-density, stable condensation is, in fact, limited by the dynamic emergence of correlated bacterial swimming.

Escherichia coli (E. coli) cells, a model for studying chemotaxis behaviors, use rotating helical filaments (flagella) that bundle at the back of the cell and propel it forward. However, during stochastic episodes of counter-rotation the bundle comes apart, causing random reorientation of the cell. These two swimming modes—forward swimming (‘run’) and random reorientation (‘tumble’)—together generate an active random walk (19). The typical run length (~10–30 μm) defines a fundamental characteristic length scale. In the presence of effector gradients, the probability of

74 tumbling is modulated to bias the random walk toward beneficial effectors and away
75 from harmful ones. In particular, bacteria can migrate towards neutral pH (20, 21), which
76 along with their ability to neutralize the environment, can lead to their spontaneous, self-
77 induced, condensation (14). Notably, this behavior is readily apparent only under
78 conditions that the bacterial suspension is coupled to larger, cell-free environment that
79 keeps the pH level within the dynamic range of efficient sensory detection, but also
80 prevents oxygen depletion, allowing cells to remain motile.

81 On the other hand, at high cell density, bacteria tend to exhibit correlated motion
82 (22, 23), which may lead to turbulent-like motion often termed 'active turbulence' (24-26).
83 This behavior arises from direct steric interactions between cells and long-range
84 hydrodynamic interactions mediated by the fluid. With notable exceptions (27, 28),
85 correlated bacterial swimming has mostly been studied in uniformly distributed
86 populations confined by physical boundaries. In contrast, bacterial condensation leads
87 to highly non-uniform cell distributions in the absence of explicit physical boundaries.
88 However, the interplay between bacterial condensation and correlated swimming is
89 poorly understood. Numerical studies have suggested that dilute self-attracting run-and-
90 tumble particles with rather weak chemotactic strength aggregate less efficiently when
91 self-induced fluid motion is considered (29). In addition, experiments have suggested
92 that cell alignment may constrain the angular rotation of individuals and thus reduce their
93 chemotactic efficiency in uniform cell density and shallow effector gradients (25).
94 However, other experiments with notable cell-density gradient have shown that the
95 tendency of cells to align may, in fact, enhance their taxis efficiency toward a local
96 source (30). Thus, how correlated, collective swimming of bacteria may influence their
97 condensation remains unclear.

98 Here, we investigate the limits of bacterial condensation using the low-pH setup
99 under conditions where oxygen deprivation or effector-saturation is not the primary

100 limiting factor. We show that stable bacterial condensation in liquid is sharply
101 constrained by the emergence of correlated bacterial swimming during cell
102 accumulation. This correlated bacterial swimming gives rise to substantial turbulent fluid
103 motion, with averaged velocity characterized by vortex-like motion with an added velocity
104 component in the outward direction aligned with the downward cell-density gradient.
105 This fluid motion effectively exerts outward physical forces on the cells that counter the
106 inward chemotaxis force. Interestingly, the alignment of the collective motion with the
107 cell-density gradient was maintained even in ring-shaped condensates (appeared at very
108 high cell densities), in which case, the bacterial behavior in the outer region of the ring
109 remained as before, but at the inner region the radial velocity and vortex direction
110 reversed. Finally, we show that in porous environments, bacterial correlated motion is
111 diminished without significantly affecting the chemotactic performance of cells.
112 Consequently, bacterial condensation is considerably enhanced, approaching the low
113 cell-density limit but with much higher cell densities.

114 Results

115 **Bacterial condensation is constrained by the emergence of correlated swimming**.
116 To test the constraints on bacterial condensation in a controlled environment, we used
117 the setup illustrated in Fig. 1B (see ref. (14)). In this setup, free-swimming cells are
118 confined within a shallow liquid layer (typically 120 μm thick), sandwiched between glass
119 and a much larger hydrogel, which establishes a uniformly low-pH environment (pH 5.2).
120 Under these conditions, bacteria tend to collectively condense due to inherent feedback
121 between the ability of the bacteria to neutralize their local pH and their chemotactic
122 ability to swim towards neutral pH (14). While cells cannot penetrate the dense hydrogel
123 mesh (3 % agarose), protons and oxygen readily diffuse across the bacterial layer and
124 into the gel, preventing their rapid depletion inside the bacterial condensate and thereby

enabling quasi-stable, high-density cell condensation (14), as demonstrated in Fig. 1B (right plot).

By following the peak cell-density (ρ_{max}) and the width at half-maximum (*W*) of the cell distribution we identified two distinct temporal phases of the condensation (Fig. 1C). Initially, in phase 1, the peak cell-density ρ_{max} increased while the width *W* decreased, reflecting strong bacterial condensation. Then, beyond a critical time point ($\mathrm{t_{sat}}$), in phase 2, the width *W* abruptly plateaued while ρ_{max} continued to rise, reflecting continued cell accumulation without further narrowing of the condensate. These trends are further demonstrated in Fig. 1D, where the width of the condensation is plotted against the maximum cell density for several repetitions. Notably, the saturated condensate width was substantially larger than the low-cell-density limit previously reported in ref. (18). The spatial profile of the bacterial accumulation also reflected this dynamical transition (Fig. 1D, inset). By normalizing each profile by ρ_{max} and the width by *W*, the profiles collapsed onto a single curve in each phase, but these cumulative curves were distinct between the two phases.

The dynamic transition described in Fig. 1D, was clearly associated with the appearance of significant density fluctuations within the condensate (Fig. 1E). Initially (phase 1), the bacterial condensate was smooth and stable (Fig. S1). However, beyond the critical time point ($\mathrm{t_{sat}}$), pronounced spatial non-uniformity developed, with clear cell-density fluctuations on a scale of approximately 20-100 μm, characterizing correlated bacterial swimming (Fig. 1E, see also Supplementary Movie 1). Analysis of these dynamic and seemingly-chaotic swimming patterns using particle image velocimetry (PIV; see Materials and Methods) revealed that, on-average (~ 30 sec), cell motion is characterized by a vortex-like clockwise rotation of the entire condensate as well as a radial component (Fig. 1E). Interestingly, the emergence of the cell-density fluctuations and correlated swimming coincided with the dynamic transition at $\mathrm{t_{sat}}$ (Fig. 1E).

151 **Fluid motion associated with the bacterial correlated swimming**. To characterize
152 the potential fluid-motion related to the bacterial correlated swimming, we embedded
153 passive green fluorescent beads (1 μm in diameter) within the bacterial population,
154 which in this case expressed red fluorescent proteins (Fig. 2). The beads' motion was
155 analyzed by particle tracking (Materials and Methods). Typically, trajectories included
156 periods of local motion interrupted by approximately directional movements, termed 'jets'
157 (Fig. 2A). To elucidate the effect of the bacterial motion on the beads, we evaluated for
158 each jet the ratio $Pe = \upsilon \cdot L/D_{beads}$ (Péclet number), where υ and L are the characteristic
159 velocity and length of the jet, respectively, and D_{beads} is the diffusion constant of the
160 beads. This *Pe* characterizes the time required for a bead to traverse a typical distance
161 by fluid flow compared to the typical diffusion time associated with the same distance.
162 The cumulative distribution of *Pe* is shown in Fig. 2A (right plot) for trajectories within
163 (green) or outside (blue) the condensate region. Clearly, the beads' motion was
164 substantially expedited within the condensate.

165 Turbulent-like fluid motion can potentially also modulate the effector (H^+)
166 distribution. To evaluate the potential significance of this effect, we evaluated the *Pe*
167 parameter for the protons ($D_{protons} \sim 10^3 \cdot D_{beads}$), assuming protons follow the local fluid
168 motion. Fig. 2B presents the cumulative number of jets per bead, integrated over a
169 diffusion time of a proton from the condensate center to its edge $t_D = W^2/4D_{H+}$, where W
170 is the width of the condensate. These data show that, on average, each bead
171 experiences at least one substantial jet with $Pe > 0.5$ over the time t_D. We therefore
172 conclude that, while cell-induced fluid motion can influence the effector distribution, it is
173 most likely not dominant.

174 As with the bacterial collective motion, averaging the beads' motion in time
175 (90 sec) reveals a vortex like fluid flow in the condensate (Fig. 2C–D). The spatial
176 distributions of the velocity components are shown in Fig. 2C, and the corresponding

177 profile of the angular velocity is shown in Fig. 2D, revealing a coordinated vortex like
178 motion. Notably, in addition to the tangential velocity contributing to vorticity, the flow
179 field exhibited a substantial outward radial component peaking at ~ 0.85 $\mu m \cdot s^{-1}$ near its
180 half-width and extended throughout the condensate. This outward radial velocity is
181 comparable to *E. coli's* chemotactic drift velocity (19, 25). Additionally, we noted that
182 above the condensed cells, which tended to occupy the lower-half region of the fluid
183 layer (~ 60 μm), the tracer beads exhibit an inward flow (Fig. 2E; Supplementary
184 Movie 2). Thus, the fluid motion in the vicinity of the condensate exhibited a three-
185 dimensional toroidal pattern (Fig. 2F).

186 **Correlated swimming leads to expulsion of non-chemotactic cells**. Given the
187 observed fluid motion, and particularly the outward radial component, we tested its effect
188 on the cells within the condensate. To this end, we repeated the condensation
189 experiments using a mixture of chemotactic (wild-type, red-labeled) and low density non-
190 chemotactic cells (*ΔcheY ΔcheZ* cells; green-labeled). Because non-chemotactic cells
191 are not subjected to the inward chemotactic force, we expected them to be more
192 sensitive to influence by the fluid motion. We found that as the wild-type cells
193 condensed, the non-chemotactic cells were expelled from the condensate (Fig. 3).
194 Additional run-and-tumble but non-chemotactic strain was tested (31), also showing
195 significant depletion, see Fig. S2 and related text. We expect this outward force to act
196 also on chemotactic cells; however, in their case, this force is balanced by an inward
197 chemotactic force that drives condensation. Still, such an outward force can be
198 expected to influence the width of the condensate.

199 **Porous environments suppress correlated swimming and enhance condensation**.
200 Porous media is expected to dampen fluid flows due to the added drag with the porous
201 scaffold (32) and potentially inhibit correlations between bacteria. For example, porous
202 media have been suggested to inhibit bioconvection (33). Thus, to further test the effect

203 of correlated swimming on bacterial condensation, we conducted experiments in which
204 cells were immersed in a thin porous environment formed by a dilute agarose hydrogel
205 (0.08%) instead of liquid (Fig. 4A). The rest of the setup was unchanged. Using the
206 channel chemotaxis assay described in ref. (21), we verified that the bacterial
207 chemotaxis performance in this porous environment was comparable to that in liquid
208 (Fig. S3). Moreover, by introducing opposing chemoeffectors at one end of the channel,
209 we triggered low cell-density accumulation. The agarose hydrogel had no detectable
210 effect on the cell-diffusion-driven broadening of this accumulation (Fig. S3).

211 In contrast, the porous environment had a dramatic effect on bacterial
212 condensation and correlated swimming (Fig. 4). Although the condensation proceeded
213 at a rate similar to that in liquid, it saturated in hydrogel only when the width of the
214 condensate approached the low-density limit of ~180 μm (18) (Fig. 4A-B).
215 Correspondingly the cell density in these tightly condensed bacterial populations
216 became extremely high. As in liquid, also in porous environment, the shape of the
217 bacterial condensate was modified when it reached its limit (Fig. S4). Finally, the
218 saturated condensates were also more compact in the vertical direction, spanning only
219 ~30 μm. Overall, in porous environments, the bacterial population spontaneously
220 condensed to its fundamental limit, reaching a cell volume fraction of 0.5-0.7 (Fig. S5),
221 while the cell population remained largely dynamic (Supplementary Video 3).

222 The enhanced condensation observed in porous environments was indeed
223 associated with a suppression of correlated swimming and associated fluid motion (Fig.
224 S6 and Fig. 4C). Furthermore, when we repeated the experiments with mixed
225 populations of chemotactic and non-chemotactic cells in the hydrogel environment, we
226 found that, despite the strong condensation of the chemotactic cells, the expulsion of the
227 non-chemotactic cells was significantly weaker (Fig. 4D). Taken together, these results

228 further support the notion that bacterial condensation in liquid media is limited by the
229 emergence of correlated swimming, rather than merely the high cell density.

230 **Ring-like condensation and the potential role of oxygen-taxis**. To test the
231 condensation at still higher cell densities, we repeated the experiments while increasing
232 the initial (uniform) cell density (Fig. 5). Since only one condensate is formed in the well
233 diameters used here (see also ref. (14)), we expect the overall cell density in the
234 condensate to increase accordingly. Yet, we find that in both liquid and porous media,
235 following the initial condensation, once enough cells accumulate, the peak density
236 ceases to increase while the condensate broadens and turns into a ring (Fig. 5). A likely
237 cause for such ring formation are the expected oxygen gradients, formed around the
238 condensate, promoting cell dispersion by oxygen-taxis (aerotaxis) (34). Compared with
239 the liquid medium, ring formation occurred at much higher cell density in the porous
240 environment but at significantly lower total number of cells (Fig. 5A). This difference
241 may result from the fact that turbulent swimming in liquid weakens the net inward force
242 and can be more easily be dominated by aerotaxis. Additionally, in liquid, aeration of the
243 condensate by bacteria-mediated convection may support the accumulation of higher
244 cell numbers prior to ring formation.

245 Interestingly, we found that in liquid, following ring formation, the vorticity
246 reverses between the inner and outer regions of the 'aerotaxis' ring (Fig. 5C). This
247 includes both the radial and tangential velocities. We note, however, that the reversals
248 of both velocities are consistent with them being determined relative to bacterial density
249 gradient: the collective motion flows radially down the cell density gradient and tends to
250 exhibit also a rightward lateral deflection in both cases (illustrated in Fig. 5C).

251 **Simplified model for condensate broadening**. To test whether the observed cell-
252 induced fluid motion (Fig. 2) can indeed lead to repulsion of non-chemotactic cells

(Fig. 3) and broaden the condensation of wild-type cells, we used Keller-Segel type chemotaxis model (35) that describes the bacterial condensation in such acidic environment (14, 36):

$$\frac{\partial \rho}{\partial t} = \vec{\nabla} \cdot \left(D \vec{\nabla} \rho - \rho \vec{v}_D \right) \qquad (1)$$

$$\frac{\partial c}{\partial t} = D_c \nabla^2 c - r_H \rho c \qquad (2)$$

Here, D is the active diffusion of the cells, v_D is their drift velocity, D_c is the effective proton diffusion coefficient, and r_H is the proton-removal rate. Note that bacteria are not growing in these experiments. Following ref. (37), the chemotaxis-induced drift velocity was modeled as $\vec{v}_D = \beta \vec{\nabla} \ln\left(c + K_{off}/c + K_{on}\right)$ where K_{on} and K_{off} are the effective dissociation constants for the chemoreceptors in the ON or OFF states, and β is the chemotaxis coefficient. The proton-removal rate was given the empirical form $r_H = \gamma c^{1/2}$ (14). The cell density dynamics was assumed to be two dimensional and radially-symmetric, occupying the top layer of a three-dimensional proton field. See Supp. Text for details and parameters used. This model accurately describes the shape of condensates in phase 1 (Fig. 6A). However, it predicts much sharper condensation and a different shape than those observed experimentally in phase 2 (Fig. 6B, dashed blue line).

Thus, considering the random fluid motion at short time scales with the added outward averaged drift component observed in Fig. 2, we suggest that bacteria subjected to such fluid motion experience not only the inward-pointing chemotactic force, but also an additional radial drift. Since this radial velocity was found to be proportional to the cell-density gradient (Figs. 2C, 5C, and S7), we added a drift velocity of the form:

$$\vec{U} = -\eta \cdot \vec{\nabla}(\rho/\rho_0) \qquad (3)$$

275 with $\eta = 10^{-7}$ cm^2s^{-1} and ρ_0 the initial (uniform) cell density ($\rho_0 \sim 0.7 \cdot 10^6$ cells·mm^2).
276 Indeed, adding this fluid-induced velocity component to the model can strictly limit the
277 condensation and account for the broadening and shape of mature condensates during
278 phase 2 (Fig. 6A-B, black lines). Notably, adding the drift velocity ($\vec{U}$) from the beginning
279 of the simulation resulted in a gradual transition between phase 1 and phase 2, which
280 does not agree with the sharp transition observed in the experiments (Figs. 1C and 6B).
281 However, adding this velocity only above a certain threshold cell density clearly account
282 for the observed transition (Fig. 6B). This is consistent with the emergence of the
283 correlated motion only above a certain cell density (Fig. 1). The added drift velocity ($\vec{U}$),
284 can also account for the expulsion of non-chemotactic cells from the condensate (Fig.
285 6C, see also Fig. 3 and Supp. Text).

286 Finally, we also considered the potential influence of correlated swimming on the
287 chemotaxis efficiency (25, 38). First we note that for such influence to limit
288 condensation, it must reduce chemotaxis efficiency. To incorporate this into the model,
289 we allowed the chemotactic coefficient (β) to depend on the local cell-density according
290 to the findings in ref. (25) (Fig. S8). Clearly, such an effect can also contribute to limiting
291 the condensation (Fig. 5B, orange line). Yet, it would not lead to repulsion of non-
292 chemotactic cells.

293 The overall relationship between the initial cell density and condensation is
294 summarized in Fig. 6D. When the initial cell density is below approximately
295 $0.4 \cdot 10^6$ cells/mm^2, no condensation is observed (14, 36). At higher densities, the initially
296 uniform distribution becomes unstable, and condensation emerges. In the absence
297 corelated swimming, the bacteria can condense until the local cell density becomes
298 sufficient to raise the local pH beyond the sensory dynamic range of the cells (blue line,
299 see also ref. (14)). However, because correlated swimming readily emerges, bacterial
300 condensation is severely restricted (simulations: dark-gray line; data: red circles). In

301 contrast, in porous media, condensation proceeds further (gray circles), though still
302 limited below the value set by the dynamic range (blue line), likely due to the non-local
303 nature of bacterial gradient sensing (see ref. (18)). At even higher cell densities,
304 condensation becomes limited by ring formation, likely due to aerotaxis (Fig. 5).

305 **Discussion**

306 Chemotaxis-mediated condensation and correlated swimming are two prominent
307 collective behaviors exhibited by motile bacteria. Here, we reveal an intrinsic interplay
308 between these behaviors. We show that bacterial condensation is fundamentally
309 constrained by the emergence of correlated swimming (Fig. 1), and, on the other hand,
310 that bacterial condensates lead to a distinct form of correlated swimming under
311 conditions of stable but sharp cell-density gradients and the absence of physical
312 boundaries confining the cell population (Figs. 1–3). Furthermore, we find that
313 correlated swimming is suppressed in porous environments, enabling exceptionally
314 robust bacterial condensation with extremely high cell density (Fig. 4).

315 The dynamics of bacterial condensation in liquid exhibit two phases (Fig. 1C-D):
316 initially, the condensate narrows while cell density increases; then, quite abruptly, the
317 width plateaus while cell density continues to rise. Notably, this transition coincides with
318 the emergence of correlated bacterial swimming (Fig. 1E), which strictly prevents further
319 narrowing of the condensate, and while additional cells can join the condensate, its width
320 remains fixed. Previous experiments demonstrated bacterial expulsion from a local
321 vortex generated by rotating magnetic microspheres at 2–40 Hz (27). Here, we show
322 that non-chemotactic bacteria are forced out of the condensate (Fig. 3), which exhibits
323 much weaker vorticity (~ 10^{-3} Hz). Notably, this expulsion force is diminished in a porous
324 environment, where cell density in the condensate is approximately 10-fold higher but
325 correlated swimming is absent (Fig. 4). This suggests that expulsion of non-chemotactic

326 cells from the condensate is not merely due to accumulation of the chemotactic cells.
327 Rather, this expulsion is consistent with the observed outward fluid flow generated by
328 correlated swimming in liquid. These forces, in turn, lead to segregation of the bacterial
329 communities into chemotactic and non-chemotactic subpopulations (Fig. 3).

330 The fluid motion in the vicinity of the condensate exhibited a three-dimensional
331 toroidal pattern (Fig. 2F). Such motion patterns seem somewhat similar to the patterns
332 observed in bioconvection (33, 39). Bioconvection occurs due to instability formed by
333 upward bacterial taxis and a downward gravitational force, which becomes dominant
334 once bacteria reach high enough cell-density. More complex behavior has been
335 observed when metallic particles were also driven up and down by the applied voltage of
336 the sample (40). In contrast, in the system described here, the condensate is overall
337 stable near the bottom surface and the fluid motion arises due to random but correlated
338 swimming of the bacteria combined with the large cell density gradients imposed by the
339 chemotactically driven condensation.

340 Advection of chemotactic effectors by the turbulent-like fluid motion may
341 contribute to limiting condensation by also limiting the buildup of steep effector gradients
342 (Fig. 2B). We find that within a time period corresponding to the diffusion time across
343 the condensate, each probe particle typically experiences at least one significant event
344 that enhances its motion beyond simple diffusion ($Pe > 0.5$). This suggests that while
345 advection might not dominate over diffusion, it is not negligible. Finally, a direct
346 influence of correlated-swimming on chemotaxis efficiency, as suggested in ref. (25),
347 may also contribute to limiting bacterial condensation (Fig. 5B). However, given the
348 strong effector and cell-density gradients within the condensates, the extent of this effect
349 is not clear.

350 In general, but with a notable exceptions (28, 41), correlated bacterial swimming
351 has been studied in uniform cell populations confined by well-defined lateral boundaries,
352 either solid (42) or at liquid–air or liquid–oil interfaces (42-45). In such settings, the
353 bacterial swimming patterns the bacterial behavior near the lateral physical boundaries
354 may play an important role in the observed behaviors (43, 46). In contrast, bacterial
355 condensation leads to stable and highly non-uniform bacterial distribution driven by self-
356 induced chemoeffector gradients in the absence of lateral boundaries. Under these
357 conditions, we find a clear radial velocity, in both the cells' correlated motion and
358 associated fluid motion, that generically aligns with the bacterial density gradient
359 (Figs. 1,2, 5 and S7). This alignment is consistent with the fact that correlated swimming
360 is enhanced at high cell densities (28) but fades as cells spread to down the density
361 gradient.

362 In small wells spanning less than few tens of microns, active turbulence was
363 shown to exhibit vortex-like motion with a random direction, whereas in larger wells,
364 chaotic motion was observed without coherent vorticity (47). In contrast, the correlated
365 swimming observed here is consistently characterized by time-averaged clockwise
366 vorticity of the entire condensate (~ 600 μm), as viewed from the glass side (Figs. 1–2).
367 At higher cell densities, when the condensate develops a ring-like structure (most likely
368 due to aerotaxis), the vorticity reverses between the inner and outer regions of the ring
369 (Fig. 5C). However, since the radial velocity also reverses across the ring, a global
370 rightward swimming tendency is maintained. Notably, this rightward swimming tendency
371 is consistent with the circular motion observed when non-interacting individual cells swim
372 near glass surfaces (< 1 μM; Fig. S9) (48). However, bacterial condensates extend
373 farther from the surface (up to 60 μm) and are far denser. Thus, it seems that the
374 interaction with the glass surface might not be enough to cause strong vorticity but it
375 may still introduce a clockwise bias to the otherwise chaotic motion.

376 Correlated bacterial swimming was clearly supressed in porous environments
377 leading to extremely dense cell condensates (Fig. 4), which may further promote the
378 formation of structured bacterial communities. Notably, experiments conducted in
379 mucin-containing media at neutral pH still exhibit correlated swimming, albeit with larger
380 vortex size (49). Interestingly, however, low-density agarose hydrogel more closely
381 resembles mucin-containing media at low pH (50), which may be more relevant to
382 certain physiological conditions than neutral pH.

383 **Materials and Methods**

384 **Strains and plasmids.** We used *E. coli* MG1655 (VF6 (31, 51)) and its derivatives
385 harboring deletion of *cheY* and *cheZ* (MK3) or deletions of all chemoreceptors and a
386 dysfunctional *cheZ* gene (non-chemotactic run-and-tumble cells (AVE4 (31)). Cells
387 expressed also a fluorescent mGFP (75 μM IPTG) or mCherry (5 mM) from a pTrc99a
388 vector (pSA11).

389 **Cell growth and motility medium.** Cells were grown over night in Tryptone Broth (TB,
390 tryptone extract 10 g/l and 5 g/l NaCl) supplemented with Ampicillin, diluted 100-fold into
391 fresh medium with IPTG, and allowed to grow at 33.5 °C with shaking. Cells were
392 harvested at an OD_{600} of 0.5 by centrifugation and gently washed twice in motility
393 medium and resuspended in motility medium with final cell concentration of OD_{600} 0.4
394 (unless otherwise mentioned). The motility medium (0.1 mM potassium phosphate,
395 0.94 mM lactic acid, 85.5 mM sodium chloride, 0.1 mM EDTA, and 1 μM methionine)
396 titrated to the desired pH with NaOH. Notably, this medium supports long-term bacterial
397 motility but not cell proliferation. Experiments in porous medium (Fig. 4) were done
398 gently mixing the cell suspension with agarose hydrogel at 37 °C to a final agarose
399 concentration of 0.08%.

400 **The condensation setup.** The setup used here is schematically illustrated in Fig. 1a.
401 For more details see ref. (14). An agarose gel (3% in motility medium) was casted in a
402 cylindrical chamber made from grade-2 titanium (6 mm height, 10.7mm diameter) and
403 sealed at the top with a mold with a thin cylindrical protrusion (~120 μm high, and radius
404 of ~ 3 or 5 mm), which will form the bacterial layer; fabricated using a resin printer
405 (Elegoo Mars 3). After the agarose solidified, the mold and the bottom cover were
406 removed and the agarose was dialyzed overnight in motility buffer and a second time, for
407 an additional 4 h, in a fresh motility buffer just before the experiment (final dialysis ratio
408 of 10^4:1). Bacterial cells were then introduced into the shallow well, suspended in either
409 liquid or soft agarose (0.08%), and the bottom and top of the chamber were covered with
410 BSA-treated glass coverslips (1% bovine serum albumin in double-distilled water for 30
411 minutes) and secured in position. Experiments were performed at room temperature (24
412 °C).

413 **Fluorescence microscopy.** The bacterial distribution was followed by using a Nikon Ti
414 microscope equipped with a 20× (0.5 NA) or 4× (0.2 NA) objective, a decoded controlled
415 stage and a 'perfect-focus' system. Large images were obtained by stitching smaller
416 images (approximately 2mm× 2mm each) with 20% overlap using a built-in function in
417 NIS Elements software (Nikon). The bacterial distribution inside the well was extracted
418 from the images by removing the measured background intensity and normalizing to the
419 average intensity within each well. Radial averaging was done by measuring the
420 fluorescence intensity around the center of focal points (Radial Profile Angle plugin for
421 ImageJ).

422 **Cell density estimates.** Due to inhomogeneity of the cell distribution in the vertical
423 direction (see Fig. 2F), cell distributions are shown in cells/mm^2. Calibration of OD_{600} to
424 cells/mm^3 was done by plating serial dilution of cells after growth (OD_{600} 0.5), yielding

425 OD_{600} 0.5 ≈ $7.2 \cdot 10^9$ cfu/mm^3. Surface density was then estimated by multiplying the cell
426 density (ρ_{3D}), averaged over the vertical direction (z), by the well height (h): $\rho = h\langle\rho_{3D}\rangle_z$.

427 **Non-uniformity estimates.** To determine the non-uniformity of the cell distribution
428 within condensates from still images, where temporal averaging is unavailable, a smooth
429 radially-averaged version of each image was subtracted from the original ones. A high-
430 pass filter was then applied to remove residual, large-scale intensity fluctuations (0-140
431 μm). Non-uniformity was then measured as the difference between the standard
432 deviation of the intensity within a disk around the condensate center (600 μm diameter)
433 and away from it.

434 **Fluorescent spheres.** In the experiments presented in Fig. 2, we used green
435 fluorescent spheres (beads) with a 1μm diameter (FluoSpheres, ThermoFisher
436 Scientific). Before use, spheres were thoroughly washed in motility medium to which
437 Tween-20 (0.01%) was added. The spheres were then added to a cell suspension,
438 which also contained Tween-20 (0.01%). The added Tween-20 prevented self-
439 aggregation of the fluorescent spheres but had no detectable effect on the bacterial
440 condensation.

441 **Particle image velocimetry (PIV).** To capture velocity fields, time-lapse fluorescent
442 images (2-10 frames per second) were captured and analyzed by PIV using PIVLab(52).
443 To analyze the collective motion of cells, a filtering procedure was first applied to remove
444 the large-scale bacterial condensation (see Non-uniformity estimates) and a nearest-
445 neighbors smoothing scheme was applied to remove residual noise. PIV analysis
446 proceeded using multipass FTT window deformation (4 passes) with the final
447 interrogation window being 16-18 pixels (64–72 μm). To avoid false detection, only
448 vectors with a correlation coefficient larger than 0.5 were kept. The PIV parameters
449 were chosen to balance between the resolution of the extracted velocity field and the

450 signal-to-noise ratio; changing them did not modify the results significantly. To analyze
451 the motion of the fluorescent beads, an initial mask was applied to ensure only particles
452 within the focal plane were analyzed. This was possible since beads within the focal
453 plane seem smaller and brighter than beads in other planes (see SI Video 3). Despite
454 the BSA treatment, beads slowly adhered to the glass coverslip. By subtracting the
455 median image from the time lapse, only non-adhered beads were analyzed. Analysis
456 then proceeded in PIVLab as described for the bacteria.

457 **Particle tracking and detection of jets.** Time lapse images (2 frames per second) of
458 the fluorescent beads were masked to ensure only particles within the focal plane are
459 analyzed (see Particle image velocimetry (PIV)). Tracking was then performed using the
460 TrackMate plugin for ImageJ. Detected tracks were exported and analyzed separately.
461 Each track was smoothed using a Savgol-Golay filter (5 frames window) and velocities
462 were estimated numerically. Jets were detected as temporal peaks in the velocity
463 magnitude with a mean prominence of more than 0.5 μm/s. The length of each track (L)
464 and it's mean velocity (v) were captured. If neighboring beads, less than L apart,
465 exhibited a jet in the same direction ($\Delta\theta < 0.15$), their jets were considered as correlated;
466 the velocity of such jets were averaged over and considered as one. Due to the low
467 density of beads, such events were rare (7 of the 2362 detected jets).

468 **Numerical solution of the model.** Solutions and parameters were based on (14) and
469 full details can be found in the Supp. Text. Briefly, the dynamics of cells was modeled in
470 2D assuming radial symmetry and the dynamics of protons was modeled in 3D
471 assuming cylindrical symmetry. Proton uptake in the bacterial layer was accounted for
472 by imposing absorbing boundary conditions for the protons at the bacterial layer
473 interface. Numerical solutions were obtained by calculating spatial derivatives with 2nd
474 order accuracy and using a 4th order Runge-Kutta method for time integration.

475 **References**

476 1. Berg HC (2004) *E. coli in Motion* (Springer, NY).
477 2. Parkinson JS, Hazelbauer GL, & Falke JJ (2015) Signaling and sensory
478 adaptation in *Escherichia coli* chemoreceptors: 2015 update. *Trends*
479 *Microbiol*. 23(5):257-266.
480 3. Colin R & Sourjik V (2017) Emergent properties of bacterial chemotaxis
481 pathway. *Curr. Opin. Microbiol*. 39:24-33.
482 4. Moore JP, Kamino K, & Emonet T (2021) Non-genetic diversity in
483 chemosensing and chemotactic behavior. *Int. J. Mol. Sci.* 22(13):6960.
484 5. Keegstra JM, Carrara F, & Stocker R (2022) The ecological roles of bacterial
485 chemotaxis. *Nat. Rev. Microbiol*.
486 6. Raina J-B*, et al.* (2022) Chemotaxis shapes the microscale organization of
487 the ocean's microbiome. *Nature* 605(7908):132-138.
488 7. Matilla MA & Krell T (2018) The effect of bacterial chemotaxis on host
489 infection and pathogenicity. *FEMS Microbiol Rev* 42(1).
490 8. Butler SM & Camilli A (2005) Going against the grain: chemotaxis and
491 infection in *Vibrio cholerae*. *Nat. Rev. Microbiol*. 3(8):611-620.
492 9. Zhou B, Szymanski CM, & Baylink A (2023) Bacterial chemotaxis in human
493 diseases. *Trends Microbiol*. 31(5):453-467.
494 10. Cremer J*, et al.* (2019) Chemotaxis as a navigation strategy to boost range
495 expansion. *Nature* 575(7784):658-663.
496 11. Adler J (1966) Chemotaxis in bacteria. *Science* 153:708-716.
497 12. Budrene EO & Berg HC (1991) Complex patterns formed by motile cells of
498 *Escherichia coli*. *Nature* 349(6310):630-633.
499 13. Budrene EO & Berg HC (1995) Dynamics of formation of symmetrical
500 patterns by chemotactic bacteria. *Nature* 376(6535):49-53.
501 14. Livne N, Koler M, & Vaknin A (2024) Collective condensation and auto-
502 aggregation of *Escherichia coli* in uniform acidic environments. *Comm. Biol.*
503 7(1):1028.
504 15. Brumley DR*, et al.* (2019) Bacteria push the limits of chemotactic precision
505 to navigate dynamic chemical gradients. *Proc. Natl. Acad. Sci.*
506 116(22):10792-10797.
507 16. Fu X*, et al.* (2018) Spatial self-organization resolves conflicts between
508 individuality and collective migration. *Nat. Comm.* 9(1):2177.
509 17. Childress S & Percus JK (1981) Nonlinear aspects of chemotaxis.
510 *Mathematical Biosciences* 56(3):217-237.
511 18. Mittal N, Budrene EO, Brenner MP, & Van Oudenaarden A (2003) Motility of
512 *Escherichia coli* cells in clusters formed by chemotactic aggregation. *Proc.*
513 *Natl. Acad. Sci.* 100(23):13259-13263.
514 19. Berg HC & Brown DA (1972) Chemotaxis in *Escherichia coli* analysed by
515 three-dimensional tracking. *Nature* 239(5374):500-504.

20. Yang Y & Sourjik V (2012) Opposite responses by different chemoreceptors set a tunable preference point in Escherichia coli pH taxis. *Mol. Microbiol.* 86(6):1482-1489.
21. Livne N & Vaknin A (2022) Collective responses of bacteria to a local source of conflicting effectors. *Sci. Rep.* 12(1):4928.
22. Toner J & Tu Y (1998) Flocks, herds, and schools: A quantitative theory of flocking. *Phys. Rev. E* 58(4):4828-4858.
23. Wensink HH*, et al.* (2012) Meso-scale turbulence in living fluids. *Proc. Natl. Acad. Sci.* 109(36):14308-14313.
24. Aranson IS (2022) Bacterial active matter. *Rep. Prog. Phys.* 85(7).
25. Colin R, Drescher K, & Sourjik V (2019) Chemotactic behaviour of *Escherichia coli* at high cell density. *Nat. Commun.* 10(1):5329.
26. Alert R, Casademunt J, & Joanny J-F (2022) Active turbulence. *Annl. Rev. Cond. Matt. Phys.* 13(Volume 13, 2022):143-170.
27. Sokolov A & Aranson IS (2016) Rapid expulsion of microswimmers by a vortical flow. *Nat. Commun.* 7(1):11114.
28. Sokolov A, Aranson IS, Kessler JO, & Goldstein RE (2007) Concentration dependence of the collective dynamics of swimming bacteria. *Phys. Rev. Lett.* 98(15):158102.
29. Lushi E, Goldstein RE, & Shelley MJ (2012) Collective chemotactic dynamics in the presence of self-generated fluid flows. *Phys. Rev. E* 86(4):040902.
30. Kai T*, et al.* (2024) Collective gradient sensing by dilute swimming bacteria without clustering. *Phys. Rev. Res.* 6(3):L032061.
31. Tamar E, Koler M, & Vaknin A (2016) The role of motility and chemotaxis in the bacterial colonization of protected surfaces. *Sci. Rep.* 6:19616.
32. Brinkman HC (1949) A calculation of the viscous force exerted by a flowing fluid on a dense swarm of particles. *Flow, Turbulence and Combustion* 1(1):27-34.
33. Bees MA (2020) Advances in bioconvection. *Annl. Rev. Fluid Mech.* 52(Volume 52, 2020):449-476.
34. Taylor BL, Zhulin IB, & Johnson MS (1999) Aerotaxis and other energy-sensing behavior in bacteria. *Annu. Rev. Microbiol.* 53:103-128.
35. Keller EF & Segel LA (1971) Traveling bands of chemotactic bacteria: a theoretical analysis. *J. Theor. Biol.* 30(2):235-248.
36. Livne N, Vaknin A, & Agam O (2025) Pattern formation in *E. coli* through negative chemotaxis: Instability, condensation, and merging. *Phys. Rev. Res.* 7(2):023095.
37. Si G, Wu T, Ouyang Q, & Tu Y (2012) Pathway-based mean-field model for *Escherichia coli* chemotaxis. *Phys. Rev. Lett.* 109(4):048101.
38. Miller M & Toner J (2024) Following your nose: Autochemotaxis and other mechanisms for spinodal decomposition in flocks. *Phys. Rev. Lett.* 132(12):128301.

39. Abe T, Nakamura S, & Kudo S (2017) Bioconvection induced by bacterial chemotaxis in a capillary assay. *Biochem. Biophys. Res. Comm.* 483(1):277-282.
40. Sapozhnikov MV, Tolmachev YV, Aranson IS, & Kwok WK (2003) Dynamic self-assembly and patterns in electrostatically driven granular media. *Phys. Rev. Let.* 90(11):114301.
41. Sokolov A, Rubio LD, Brady JF, & Aranson IS (2018) Instability of expanding bacterial droplets. *Nat. Commun.* 9(1):1322.
42. Nishiguchi D, Aranson IS, Snezhko A, & Sokolov A (2018) Engineering bacterial vortex lattice via direct laser lithography. *Nat. Commun.* 9(1):4486.
43. Wioland H, Woodhouse FG, Dunkel J, Kessler JO, & Goldstein RE (2013) Confinement stabilizes a bacterial suspension into a spiral vortex. *Phys. Rev. Lett.* 110(26):268102.
44. Vincenti B*, et al.* (2019) Magnetotactic bacteria in a droplet self-assemble into a rotary motor. *Nat. Commun.* 10(1):5082.
45. Nishiguchi D, Shiratani S, Takeuchi KA, & Aranson IS (2025) Vortex reversal is a precursor of confined bacterial turbulence. *Proc Natl Acad Sci U S A* 122(11):e2414446122.
46. Lushi E, Wioland H, & Goldstein RE (2014) Fluid flows created by swimming bacteria drive self-organization in confined suspensions. *Proc. Natl. Acad. Sci. (USA)* 111(27):9733-9738.
47. Nishiguchi D, Shiratani S, Takeuchi KA, & Aranson IS (2025) Vortex reversal is a precursor of confined bacterial turbulence. *Proc. Natl. Acad. Sci. USA* 122(11):e2414446122.
48. Lauga E, DiLuzio WR, Whitesides GM, & Stone HA (2006) Swimming in circles: motion of bacteria near solid boundaries. *Biophys J* 90(2):400-412.
49. Liao W & Aranson IS (2023) Viscoelasticity enhances collective motion of bacteria. *PNAS Nexus* 2(9).
50. Celli J*, et al.* (2005) Viscoelastic properties and dynamics of porcine gastric mucin. *Biomacromolecules* 6(3):1329-1333.
51. Frank V, Piñas GE, Cohen H, Parkinson JS, & Vaknin A (2016) Networked chemoreceptors benefit bacterial chemotaxis performance. *mBio* 7(6).
52. Thielicke W & Sonntag R (2021) Particle Image Velocimetry for MATLAB: Accuracy and enhanced algorithms in PIVlab. *J. Open Res. Soft.*

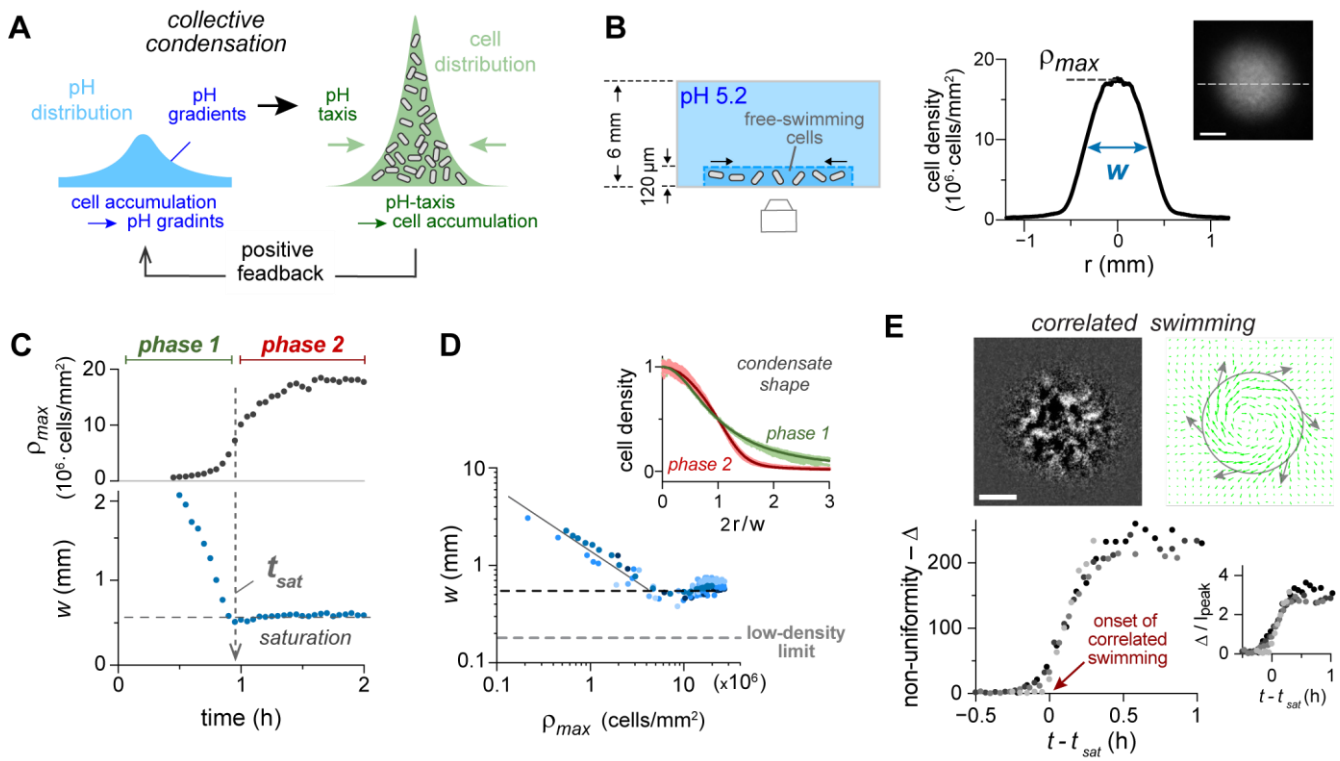

Figure 1. Bacterial condensation is constrained by correlated swimming. (A) Schematic of bacterial condensation in acidic environments (see ref. 14). On the one hand, by neutralizing free protons in their vicinity, cells generate pH gradients in an otherwise uniform acidic environment. On the other hand, cells are chemotactically attracted toward neutral pH. These behaviors form reinforcing feedback that derives condensation. **(B)** The experimental setup consists of a thin liquid layer (~ 120 µM thick and 5 mm diameter) with GFP-expressing, free-swimming bacteria, molded in a 3% agarose gel. Both the liquid layer and the surrounding gel initially formed a uniform acidic environment (pH 5.2), and the bacterial condensation dynamic was monitored using fluorescence microscopy. A typical condensate at steady state is shown on the right (2 h after initiation, scale bar - 300 µm) along with the radially averaged cell-density. The width at half maximum (w) and peak cell density (ρ_{max}) are marked. **(C)** A typical condensation dynamic is shown, characterized by the width (w) and peak cell density (ρ_{max}). The abrupt saturation of the condensate's width is marked by t_{sat}. **(D)** The width of the condensate (w) is plotted against peak cell density for 7 independent experiments. Solid gray line reparents power-law slope of -2/3. Dashed lines mark the width of saturated condensates (dark gray) and the corresponding value measured at low cell density (light gray, (18)). *Inset* – normalized cell density profiles observed at different time points for 3 independent experiments: profiles were labeled red for $t < t_{sat}$ and green for $t > t_{sat}$. Profiles at $t \sim t_{sat}$ (within 5 min) are not shown. Density was normalized by subtracting the baseline and dividing by the peak density; the radial coordinate was normalized by $w/2$. **(E)** Collective swimming emerges at $t \sim t_{sat}$. A typical filtered fluorescence image (top-left) highlighting the emerging non-uniformity (see Materials and Methods), and the corresponding time-averaged (30 s) velocity field obtained by particle image velocimetry (PIV; top-right; grey arrows are a guide to the eye). See also SI Video 1. Fluorescence intensity of the non-uniformity (Δ) within condensates (r ≤ 300 µm) is shown over time (lower plot; 4 independent experiments. see Materials and Methods); inset – Δ divided by the square root of the peak intensity (I_{peak}). Note that the onset of this non-uniformity occurs at $t \sim t_{sat}$.

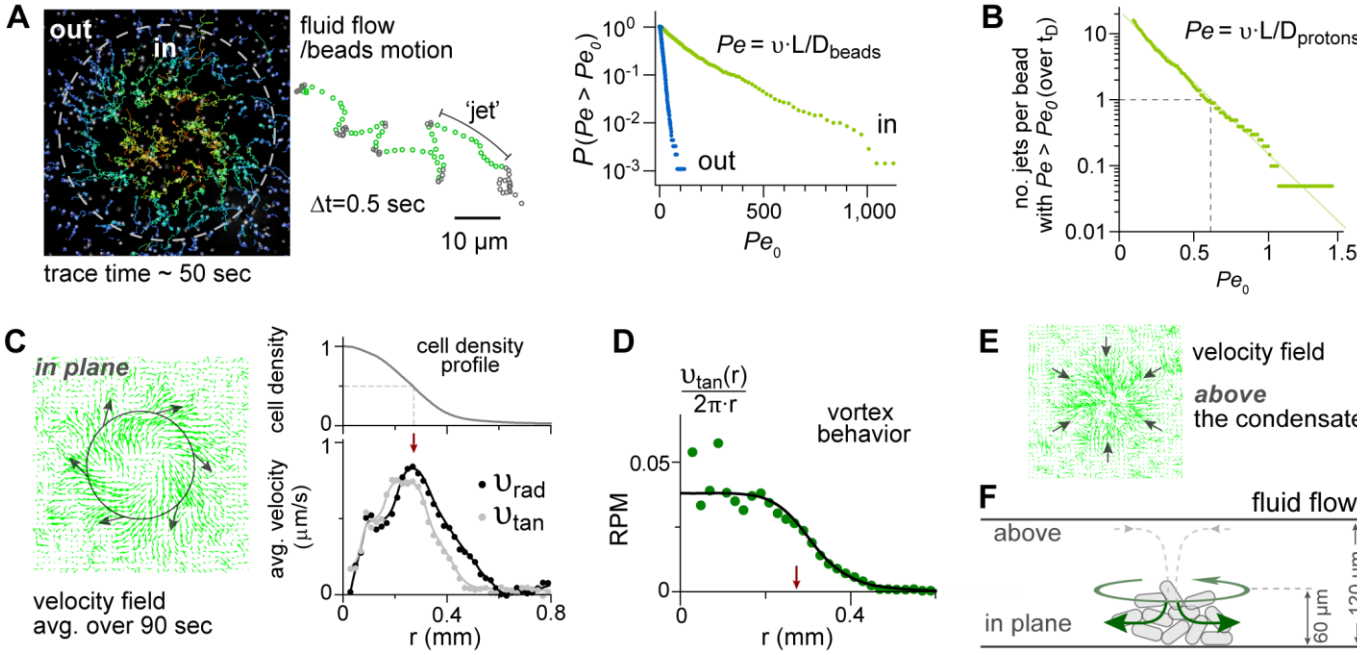

Figure 2. Fluid motion within the condensate. Fluid motion was assessed by tracking green fluorescent beads (1 μm diameter) mixed with the bacterial cells (red-labeled). (**A**) Motion of beads in the condensate plane. Image shows the traces of individual beads tracked over 50 sec using particle tracking analysis (Materials and Methods). The dashed white circle indicates the condensate width (~ 550 μm). A typical trace is highlighted on the right, illustrating intermittent motion composed of periods of local random motion (gray symbols) and periods of directed motion, termed 'jets' (green symbols). The length (*L*) and average speed (*υ*) of each jet were used to calculate $Pe = \upsilon \cdot L/D_{beads}$, with $D = 5 \cdot 10^{-9}$ cm^2 s^{-1}. The cumulative distribution of this parameter is shown in the right plot for beads within or outside the condensate, clearly demonstrating enhanced motion within the condensate. (**B**) Comparison of the beads motion to proton diffusion, using $D_{H+} = 5 \cdot 10^{-6}$ cm^2 s^{-1}. Beads traces (90 sec long) were analyzed. Plotted is the number of jets per bead whose *Pe* value exceeds a given threshold (Pe_0) during the diffusion time across the condensate $t_D \sim w^2/4D_{H+}$. (**C**) Time-averaged velocity field (90 sec) in the condensate plane, extracted using PIV (Materials and Methods). Profiles of the radial and tangential velocity components are shown on the right alongside the corresponding (normalized) cell density profile. The red arrow marks the condensate width (w) (**D**) The angular velocity profile, revealing correlated vortex-like motion. (**E**) Measured velocity field above the condensate showing a radially-inward flow. (**F**) Schematic summarizing the inferred fluid flow in the vicinity of the condensate (see also Supplementary Video 2).

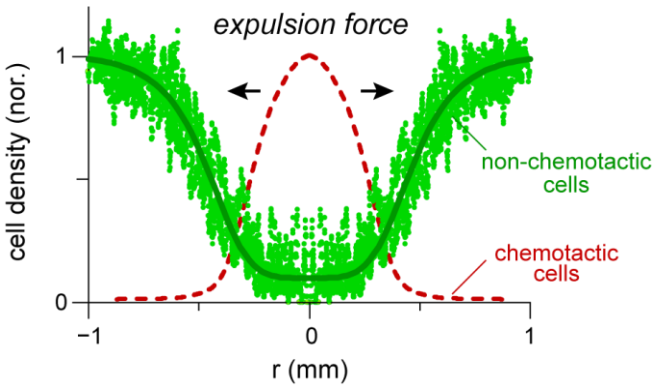

Figure 3. Correlated swimming forces non-chemotactic cells out of the condensate. Cell-density profiles of chemotactic cells (red line) and non-chemotactic, smooth-swimming cells (green symbols) in a mature condensate. Profiles were normalized to the background density and divided by a factor of 3000 (red) and 1 (green). The chemotactic and non-chemotactic bacteria, labeled in red and green fluorescence, were initially mixed in a 100:1 ratio, respectively, and applied to the setup shown in Fig. 1B (Materials and Methods; 3 independent experiments).

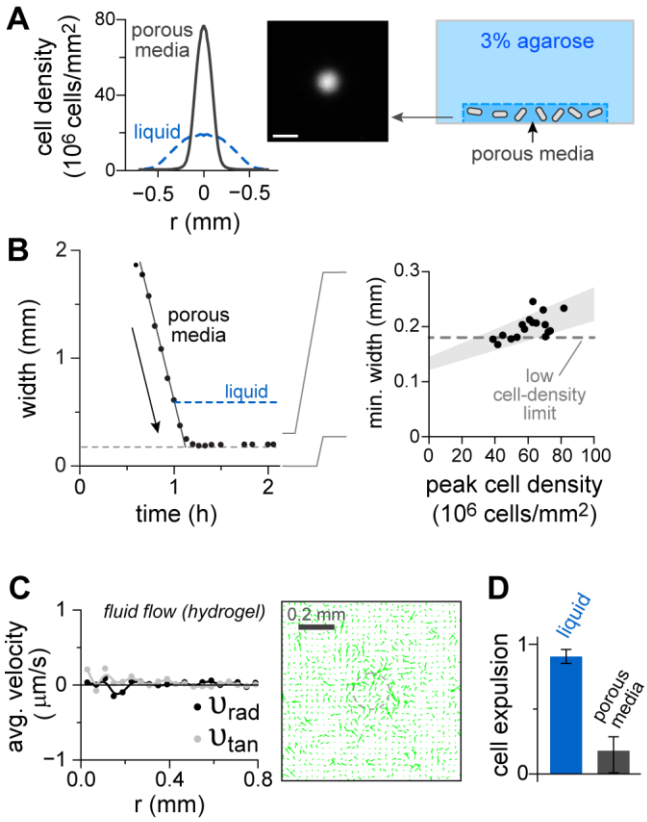

Figure 4. Bacterial condensation in porous media. Experiments similar to those described in Fig. 1 were performed except that cell were suspended in a porous medium (0.08% agarose hydrogel) rather than liquid medium. **(A)** Representative mature condensates in porous (gray) or liquid (blue) media. Typical fluorescence image of the condensate in porous medium (scale bar 300 μm) and a schematic description of the revised setup are also shown. The layers dimensions are similar to those in Fig. 1, with 3 mm diameter. **(B)** The condensation dynamics (width versus time) in porous medium (left plot, black symbols). The saturation width value in liquid is marked with dashed blue line. *Inset* – The saturation width values in porous medium for 17 different experiments are plotted against the saturated peak cell density. The saturation width at low cell-density (ref. (18)) is marked with gray dashed lines. Gray region shows a linear fit to the data. **(C)** Fluid flow in the plane of a condensate in porous medium (analyzed by PIV; see Materials and Methods). The velocity field (right) and the radial and tangential velocities (left) were averaged over 30 s. **(D)** Expulsion of non-chemotactic cells from the condensate for experiments done in liquid (from Fig. 3) or porous media.

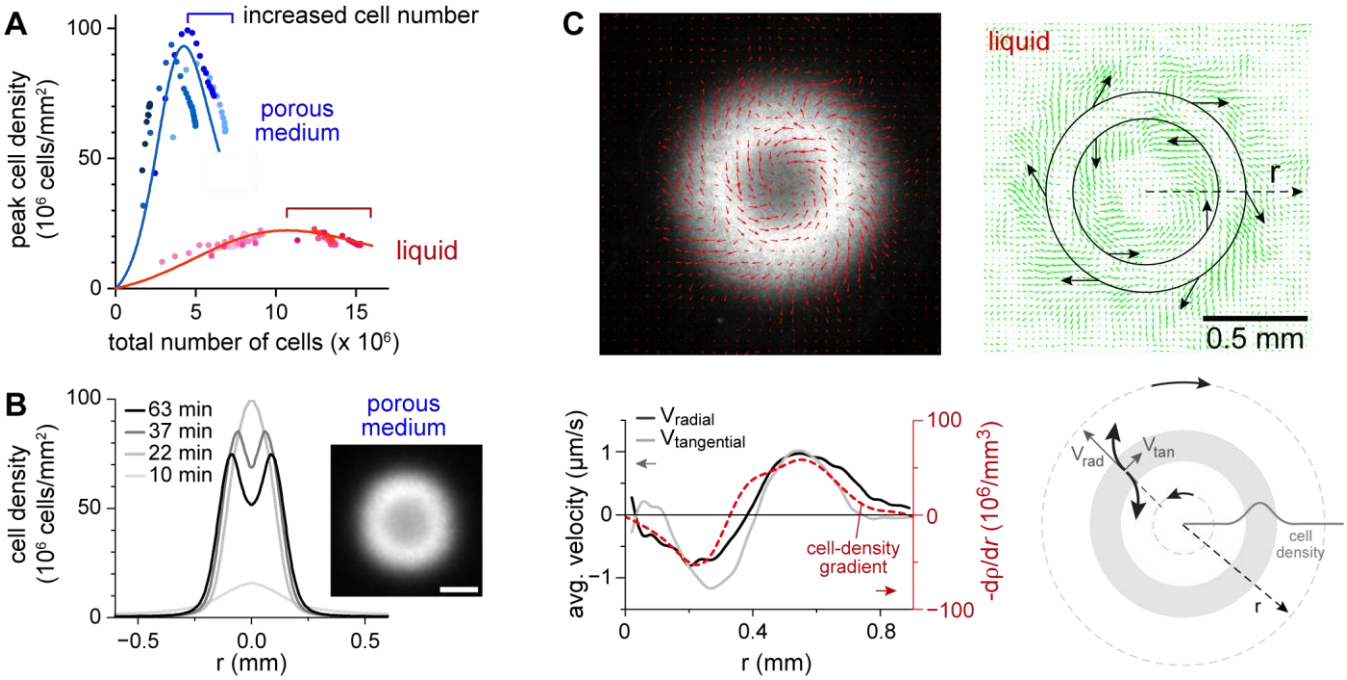

Figure 5. Condensation at still higher cell number. (A) The maximal cell density is plotted against the total number of cells in the condensate for experiments with the cells in liquid (red symbols) or porous medium (blue symbols). Notably, this maximal cell density falls at high cell numbers—controlled by the initial (uniform) cell density—due to formation of ring-shaped cell distribution, shown in (B) for cells in porous medium and (C) for liquid. **(B)** Evolution of the condensate profile in porous medium. A snapshot image at 50 min is also shown demonstrating the ring formation (scale bar – 150 μm). **(C)** A snapshot image of a mature condensate at high cell number in liquid. The bacterial time-averaged velocity fields (extracted using PIV) are overlaid on the image (red arrows), and demonstrated on the right (green arrows). The profile of time-averaged radial and tangential velocities is shown below the image, along with the cell density gradient; note that both velocities reverses across the ring. This reversal is also schematically described on the right.

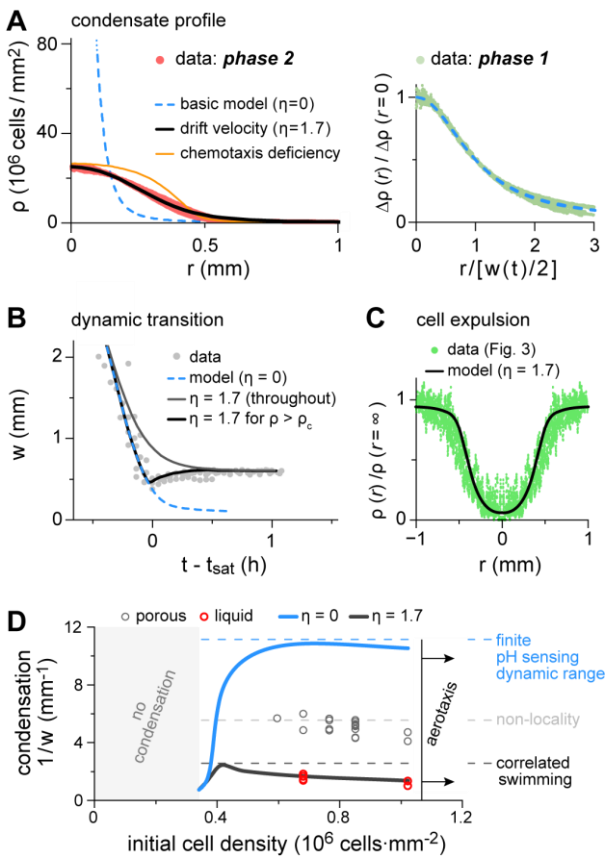

Figure 6. Simplified model for condensate broadening by collective motion. (A) Measured condensate profiles of 3 independent experiments in liquid medium (markers) compared with numerical solutions of the Keller-Segel type model in phase 1 (right) and phase 2 (left). Dashed blue line represents the basic model ($\eta = 0$), which saturate only due to the limited sensory dynamic range of the cells. Expulsion force was modeled by adding drift velocity $\vec{U} = -\eta\vec{\nabla}(\rho/\rho_0)$ (black line; $\eta = 1.7 \cdot 10^{-7}$ cm^2 s^{-1}). Alternatively, following ref. 25, the chemotaxis efficiency was allowed to depend on the local cell-density (orange line). (B) Condensation dynamics. Condensate width plotted against t-t_{sat} for 4 independent experiments (gray symbols) along with the simulated width of the different models (as labeled). To simulate the emergence of correlated motion above ρ_c, a sigmodal function was used $(1 + \exp(-(k/\rho_0)(\rho_{max} - \rho_c)))$ with $k = 3$ and $\rho_c = 25\rho_0$ (~17·10^6 cells·mm^{-2}). (C) Expulsion of non-chemotactic cells (ρ_{NC}) by condensating wild-type cells (ρ_{WT}). Data from Fig. 3 of ρ_{NC} is replotted along with the distribution predicted by the model: $\rho_{NC} = \exp\left(-\frac{\eta}{D_{NC}}\frac{\rho_{WT}(r)}{\rho_0}\right)$ with D_{NC} = 2.5·10^{-6} cm^{2}s^{-1}, η = 1.7·10^{-7} cm^{2}s^{-1} and $\rho_{WT}(r)$ taken from the experimental data in (A). (D) Summary of the saturated condensation (defined here as 1/W) as a function of the initial cell density. Data from various experiments is shown as empty circles and simulations are shown as lined (as labeled). The 'aerotaxis' line marks the density above which aerotaxis rings become dominant. The low-density limit (18) is plotted as a dashed gray line ('non-locality'). In the 'no condensation' region the initially-uniform cell distribution is stable (14, 36). See Text and Supp. Text for details.